Journal of Materials Chemistry C

PAPER

View Article Online
View Journal | View Issue

Check for updates

Cite this: J. Mater. Chem. C, 2018, 6, 4523

Interfacial electronic states and self-formed p–n junctions in hydrogenated MoS_2/SiC heterostructure†

Qinglong Fang,[a] Xumei Zhao,[b] Yuhong Huang,[c] Kewei Xu,[ad] Tai Min,[a] Paul K. Chu*[e] and Fei Ma*[ae]

Received 10th February 2018,
Accepted 31st March 2018

DOI: 10.1039/c8tc00742j

rsc.li/materials-c

It is difficult to generate p–n junctions in atomically thin transition metal dichalcogenides (TMDs) because of the great challenge of selective doping. First-principles calculations demonstrate that the electronic states in monolayer MoS_2 could be substantially tuned through contact with hydrogenated SiC sheets, as a result of interface-induced electronic doping. Specifically, monolayer MoS_2 exhibits metallic characteristics when put in contact with the Si termination of SiC–H (MoS_2/SiC–H), but exhibits ambipolar type polarization when in contact with the C termination of CSi–H (MoS_2/CSi–H). Furthermore, monolayer MoS_2 can be switched from p-type on H–Si terminations (MoS_2/H–SiC and MoS_2/H–SiC–H) to n-type on H–C terminations (MoS_2/H–CSi and MoS_2/H–CSi–H). Accordingly, p–n junctions can be generated in bilayer MoS_2 if a fully hydrogenated monolayer SiC is inserted between the layers. In addition, the staggered band alignment of the top and bottom monolayers of MoS_2 leads to considerable rectification of current. The results are helpful for the design of TMD based nanoelectronic devices.

Published on 05 April 2018. Downloaded by Xian Jiaotong University on 12/26/2019 10:34:25 AM.

1. Introduction

Two-dimensional (2D) crystals exhibit new physics and potential applications in novel devices.[1–4] Up to now, a great number of 2D materials, such as molybdenum disulfide (MoS_2),[5–8] boron nitride (BN),[9] silicon carbide (SiC),[10,11] and black phosphorus,[12,13] have been successfully fabricated, which has greatly stimulated research interest in academic society. Compared to its bulk counterpart, monolayer MoS_2 is a direct-band-gap semiconductor with a band-gap of 1.8 eV,[14] high carrier mobility and high on/off ratio.[6,14] Moreover, it is abundant in nature and could be fabricated at a large scale.[15] Thus, a wide variety of MoS_2 have been used as active materials to fabricate atomically thin field-effect transistors (FETs),[14,16] integrated circuits,[17,18] light-emitting diodes, solar cells, and photodiodes.[19–21]

The p–n diodes represent the most fundamental building blocks for applications. Commonly, MoS_2 exhibits n-doping owing to sulfur vacancies, and the lack of p-type doping limits its applications in electronic devices. Compared to traditional semiconductors, it is particularly difficult to generate p–n diodes in atomically thin MoS_2 due to the challenges of selective doping. However, nearly all the atoms in monolayer MoS_2 can "feel" the surface and interface, and the fundamental physics should be strongly sensitive to the surface and interface configuration. For example, an atomically thin p–n junction is generated in bilayer MoS_2/WSe_2 heterostructures fabricated by chemical vapor deposition (CVD).[22–25] The different work function and band gap between these two monolayers lead to an atomically sharp heterointerface with type-II band alignment, but with a lower photovoltage.[26,27] Interestingly, it was predicted that an asymmetrical functionalization might be induced in graphene by adsorption of H and F and, consequently, monolayer MoS_2 can be switched from n- to p-type or *vice versa*.[28] The hydrogenation sites and stacking patterns are crucial for modulating the physical properties of monolayer MoS_2/AlN.[29] Hence, it is fundamentally important to exploit suitable contact materials so that the interfacial electronic states and the physical properties of monolayer MoS_2 could be well controlled.

Silicon carbide (SiC) is an important substrate for the fabrication of electronic devices adopted in extreme conditions. Monolayer SiC is a nonmagnetic semiconductor with a band

[a] State Key Laboratory for Mechanical Behavior of Materials, Xi'an Jiaotong University, Xi'an 710049, Shaanxi, China. E-mail: mafei@mail.xjtu.edu.cn
[b] College of Materials Science and Engineering, Shaanxi Normal University, Xi'an 710062, Shaanxi, China
[c] College of Physics and Information Technology, Shaanxi Normal University, Xi'an 710062, Shaanxi, China
[d] Department of Physics and Opt-electronic Engineering, Xi'an University of Arts and Science, Xi'an 710065, Shaanxi, China
[e] Department of Physics and Department of Materials Science and Engineering, City University of Hong Kong, Tat Chee Avenue, Kowloon, Hong Kong, China. E-mail: paul.chu@cityu.edu.hk

† Electronic supplementary information (ESI) available. See DOI: 10.1039/c8tc00742j

Published on 05 April 2018. Downloaded by Xian Jiaotong University on 12/26/2019 10:34:25 AM.

gap of 2.53 eV, high stability and large in-plane stiffness.[10,30] Rajan *et al.*[31] illustrated the direct growth of high-quality few-layer MoS_2 on SiC by a solvothermal reaction, and they found that the heterostructures exhibit rectification characteristics. Gou *et al.*[32] fabricated a flower-like MoS_2–SiC hybrid structure by a solvothermal reaction and the hybrid structure exhibits enhanced hydrogen evolution properties. Hydrogenation is an effective approach for changing the electronic states.[33–35] The lattice constants of monolayer SiC and hydrogenated SiC are 3.10 Å and 3.13 Å, respectively. Since Si and C terminations on SiC exhibit different bonding states with H atoms,[36] monolayer MoS_2 on hydrogenated SiC with Si and C terminations should possess distinct interfacial electronic states and physical properties. In this paper, first-principles calculations are done to study the influences of hydrogenation on the interfacial electronic states of MoS_2/SiC. It was found that the electronic states of monolayer MoS_2 depend on the surface termination of SiC after hydrogenation, which might be changed from n-type to p-type or even to metal. Furthermore, a p–n junction could be generated if the fully hydrogenated monolayer SiC is sandwiched between two monolayer MoS_2. The results are helpful in the design and fabrication of TMD-based new-concept devices.

2. Computational details

First-principles calculations based on density functional theory were carried out by using the Vienna *ab initio* simulation package (VASP).[37,38] The projector augmented wave (PAW) method[39] was used to describe the electron–ion core interaction, which is more accurate than the ultra-soft pseudopotentials. Commonly, the Perdew–Burke–Ernzerhof (PBE)[40] method underestimates the band gap of semiconductors; thus the gap values should be corrected by a hybrid functional, in which the Hartree–Fock exchange is included. So we have checked the reported results by using PBE and HSE06. It is found that the calculation results are material dependent. As for bulk MoS_2, the measured band gap is 1.29 eV;[41] however, Botti *et al.*[42] calculated band gaps of 0.87 eV and 1.42 eV by using PBE and HSE06 methods, respectively. As for monolayer MoS_2, Mak *et al.*[6] reported a band gap of 1.90 eV *via* optical spectroscopy measurement, but Lebègue *et al.*[43] and Ataca *et al.*[44] reported band gaps of 1.78 eV and 2.23 eV by using PBE and HSE06 methods, respectively. Obviously, the PBE method underestimates the band gap of both bulk and monolayer MoS_2, while the hybrid functional overestimates the band gap.[45] Tran *et al.*[46] and Singh *et al.*[47] found that the PBE and HSE06 methods provide the same variation trend of band gaps for different materials or for one material but under different pressures. So the PBE and HSE06 calculations only influence the specific values of band gaps but have little influence on the variation trend.[45–47] Since the calculations by the HSE06 method will cost an extremely long computing time, the PBE formulation of the generalized gradient approximation (GGA) was chosen to describe the exchange–correlation interaction. Since semi-local functionals, such as GGA, fail to describe weakly interacting systems, the van der Waals interaction in the Grimme approach was adopted to describe the weak interlayer interaction.[48] The cutoff energy for the plane-waves was chosen to be 450 eV. The Brillouin-zone integration was performed by using an $11 \times 11 \times 1$ *k*-mesh according to the Monkhorst–Pack scheme, and Gaussian smearing broadening of 0.05 eV was adopted. To avoid artificial interactions between the periodic images of the structures, a vacuum region of at least 15 Å was used. A conjugate-gradient algorithm was employed to relax the ions to the ground states with an energy convergence of 1.0×10^{-5} eV and a force convergence of 0.02 eV Å^{-1} on each ion. Visualizations of supercells and structures were made with VESTA software.[49]

The transport properties were calculated using the Atomistix Toolkit (ATK) package based on the non-equilibrium Green's function (NEGF) method combined with DFT calculations.[50,51] The two-probe configuration was used to simulate the device with Au as the electrodes. The electrodes and the central regions were separately optimized, in which supercell models with a vacuum space of at least 15 Å in thickness were adopted. The single zeta polarized (SZP) basic set was adopted. A force convergence of 0.01 eV Å^{-1} and an energy convergence of 1×10^{-5} eV per atom were adopted. The density mesh cutoff of 150 Ry was chosen to balance the calculation efficiency and accuracy. The *k*-points of the electrodes and the central region were set to $20 \times 20 \times 100$ and $20 \times 20 \times 1$, respectively, in the Monkhorst–Pack scheme. The transmission coefficient $T^{k_\parallel}(E)$ (where $k_\parallel$ is a reciprocal lattice vector along an in-plane direction) was calculated as follows:

$$T^{k_\parallel}(E) = \mathrm{Tr}\left[\Gamma_{\mathrm{L}}^{k_\parallel}(E) G^{k_\parallel}(E) \Gamma_{\mathrm{R}}^{k_\parallel}(E) G^{k_\parallel\dagger}(E)\right], \qquad (1)$$

in which $G^{k_\parallel}(E)$ is the retarded Green's function and $\Gamma_{\mathrm{L/R}}^{k_\parallel}(E) = i\left(\sum_{\mathrm{L/R}}^{r,k_\parallel}(E) - \sum_{\mathrm{L/R}}^{a,k_\parallel}(E)\right)$ represents the level broadening due to left and right electrodes in terms of the self-energies of the electrodes, $\sum_{\mathrm{L/R}}^{k_\parallel}(E)$.[52] The transmission function at a given energy $T(E)$ is averaged over different $k_\parallel$ in the irreducible Brillouin zone.

The binding energy (E_b) is defined as $E_b = (E_h - E_{MoS_2} - E_s)/N_S$, in which E_h, E_{MoS_2} and E_s are the free energies of the heterostructure, free-standing MoS_2 and the SiC nanosheet. N_S is the number of S atoms in the supercell. The system is stable for negative E_b, and the smaller the E_b value, the stronger the heterostructure binding. The Mulliken charge distribution, including atomic charge, bond population, and charge transfer in the heterostructures, is analyzed by using a projection of a linear combination of atomic orbitals. To gain further insight into the bonding nature and interlayer interaction, the plane-averaged charge density difference, $\Delta\rho = \rho_h - \rho_{MoS_2} - \rho_s$, is calculated, in which ρ_h, ρ_{MoS_2}, and ρ_s are the plane-averaged charge densities of the heterostructure, MoS_2, and SiC nanosheet.

 This journal is © The Royal Society of Chemistry 2018

Published on 05 April 2018. Downloaded by Xian Jiaotong University on 12/26/2019 10:34:25 AM.

3. Results and discussion

3.1. Structural stability

An infinite 2D MoS_2/SiC heterostructure is constructed by stacking monolayer MoS_2 and SiC on each other. The optimized lattice constants of the $4 \times 4 \times 1$ supercells of monolayer MoS_2 and SiC are 3.190 Å and 3.096 Å, respectively (Fig. S1, in the ESI†), which show good consistency with the experimental and theoretical results.[3,36] The optimized Mo–S bond length in the monolayer MoS_2 is 2.413 Å, and monolayer SiC as an analog of graphene has a bond length of 1.787 Å, and nearly all the atoms are in the same plane (Table S1, ESI†). $4 \times 4 \times 1$ supercells of an SiC/MoS_2 heterostructure with a lattice mismatch of 1.2% are established, in which the lattice constant of MoS_2 is slightly compressed but that of SiC is stretched. It was reported that the direct band gap is maintained and the band gap is reduced from 1.9 eV to 1.6 eV as the lattice constant is increased from 3.119 Å to 3.169 Å for the monolayer MoS_2.[53] A strain of at least 1.6% is needed to induce substantial change in the electronic states of MoS_2. So the influence of mismatch strain on the electronic states of the MoS_2/SiC heterostructure is negligible.

van der Waals heterostructures are typically fabricated by mechanical exfoliation and subsequent attachment, so the orientation cannot be well controlled. For an MoS_2/SiC heterostructure, the six most likely stacking configurations are explored, as shown in Fig. S2 (ESI†). The rotation angles of monolayer MoS_2 with respect to monolayer SiC are 0°, 60°, 120°, 180°, 240° and 300°. Fig. S3 (ESI†) shows the calculated binding energies, and the heterostructure of configuration *d* is the most stable with a binding energy of −144 meV per S atom. Furthermore, the binding energy is much lower than that of monolayer MoS_2 on silicene (−64 meV) or on germanene (−71 meV).[54] The interlayer separation (d_0) in the MoS_2/SiC heterostructure of configuration *d* is 2.928 Å, illustrating physical adsorption between them. Therefore, MoS_2 is bonded to monolayer SiC *via* van der Waals interaction or electronic interaction, but not orbital hybridization. The structural and electronic properties of all the configurations are almost the same. So only configuration *d*, as shown in Fig. 1a, is considered in the following.

Since each partially hydrogenated SiC has two terminations, there are four types of stacking configurations of MoS_2 on partially hydrogenated SiC (Fig. S4a and b, ESI†). For H–SiC, MoS_2 can be contacted with the C termination of H–SiC (labeled MoS_2/CSi–H, Fig. 1b) and the H terminated side of H–SiC (labeled MoS_2/H–SiC, Fig. 1c); for SiC–H, MoS_2 can be in contact with the Si termination (labeled MoS_2/SiC–H, Fig. 1d) and the H terminated side (labeled MoS_2/H–CSi, Fig. 1e). The Mo–S bond length is the same as that in monolayer MoS_2, but the Si–C, Si–H, and C–H bond lengths are slightly lengthened (Table S1, ESI†). As compared to MoS_2 on SiC, the d_0 value is shortened, especially for the MoS_2/SiC–H heterostructure, implying enhanced interlayer interaction. As listed in Table 1, the binding energies of MoS_2 on H–SiC (MoS_2/CSi–H and MoS_2/H–SiC) are higher than those of MoS_2 on SiC–H (MoS_2/SiC–H and MoS_2/H–CSi). Moreover, the binding energies of MoS_2 on partially hydrogenated SiC are higher than those of MoS_2 on SiC by 200–700%; that is, partial hydrogenation enhances the interaction between MoS_2 and SiC, and thus improves the structural stability of monolayer MoS_2 on SiC. For MoS_2 on fully hydrogenated SiC (labeled H–SiC–H),[55] there are two kinds of heterostructures, labeled MoS_2/H–SiC–H (Fig. 1f) and MoS_2/H–CSi–H (Fig. 1g). The calculated structural parameters are also summarized in Table 1, and little difference in structural properties and binding energies is in evidence. As compared to monolayer MoS_2 on SiC and on partially hydrogenated SiC, the structure of monolayer MoS_2 on fully hydrogenated SiC changes little. Although the interlayer separation of MoS_2 and fully hydrogenated SiC is reduced, the binding

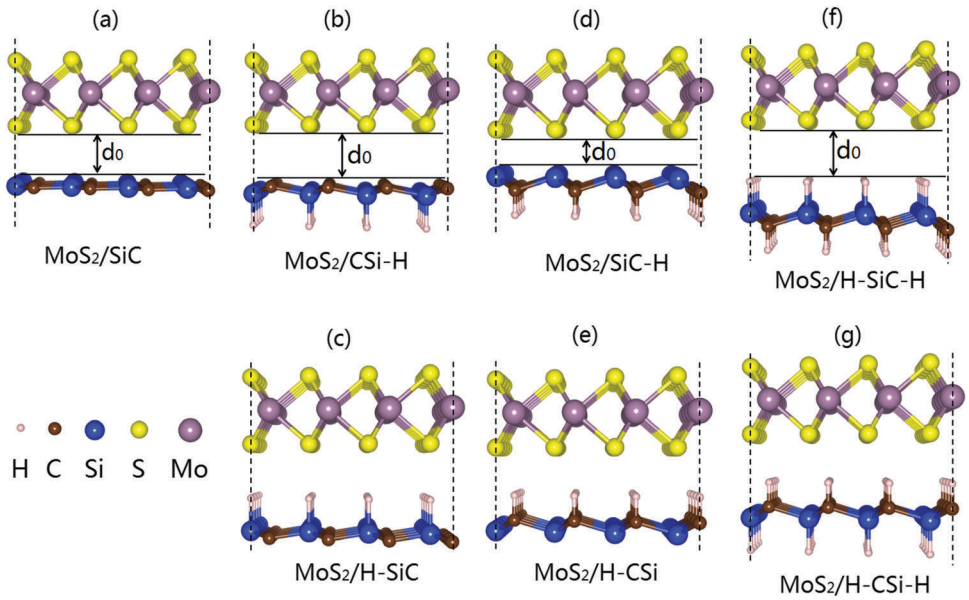

Fig. 1 Schematic illustration of monolayer MoS_2 on an SiC sheet with and without hydrogenation.

Published on 05 April 2018. Downloaded by Xian Jiaotong University on 12/26/2019 10:34:25 AM.

Table 1 Bond lengths of Mo–S (L_{Mo-S}), Si–C (L_{Si-C}), C–H (L_{C-H}), and Si–H (L_{Si-H}), interlayer distance d_0 (Å), buckling height h (Å), and binding energy E_b (meV) of monolayer MoS_2 on SiC with or without hydrogenation

Configuration	L_{Mo-S} (Å)	L_{Si-C} (Å)	L_{Si-H} (Å)	L_{C-H} (Å)	d_0 (Å)	h (Å)	E_b (meV)
MoS_2/SiC	2.401	1.808			2.928		−144
MoS_2/CSi–H	2.408	1.866	1.522		2.975	0.370	−188
MoS_2/H–SiC	2.406	1.852	1.534		2.556	0.286	−426
MoS_2/SiC–H	2.401	1.911		1.116	2.174	0.579	−1273
MoS_2/H–CSi	2.401	1.911		1.116	2.174	0.579	−1273
MoS_2/H–SiC–H	2.404	1.906	1.110	1.493	2.924	0.567	−153
MoS_2/H–CSi–H	2.405	1.905	1.108	1.493	2.245	0.562	−185

energy in MoS_2 on fully hydrogenated SiC is close to that in MoS_2 on SiC.

3.2. Charge transfer and redistribution

The interlayer interaction from MoS_2 is through the charge redistribution in the heterostructure.[56,57] In order to investigate the electronic properties of MoS_2 on SiC with or without hydrogenation, the planar-averaged charge density difference along the z-direction is calculated, as depicted in Fig. 2. As is well known, the charge redistribution might lead to polarization as well as the formation of an interface dipole. The interface charge depletion is direct evidence of a surface charge repulsion effect. According to Mulliken charge analysis, 0.091 e is transferred from the SiC sublayer to the MoS_2 sublayer and the holes remain in the SiC sublayer (Fig. 2a). This charge redistribution induces a built-in electric field across the heterostructure, and hinders the diffusion of electrons and holes, and finally a balance is established. For MoS_2 on the hydrogenated SiC, the charge transfer from SiC to MoS_2 is not considerable except for the MoS_2/SiC–H heterostructure (Fig. 2b and c). Similar results were found in MoS_2 on decorated AlN nanosheets.[29] For MoS_2 on H–SiC, the charge in the interface is close to the MoS_2 sublayer, but the charge is close to SiC–H for MoS_2 on SiC–H. The maximum $\Delta\rho$ in MoS_2/SiC–H is larger than those of MoS_2/CSi–H, MoS_2/H–SiC, and MoS_2/H–CSi by 300% or so (Fig. 2b), which is consistent with the changes in the interlayer separation and binding energy, as listed in Table 1. Commonly, the stronger the interaction between sublayers, the more charge transfer occurs. The d_0 is only 2.174 Å, which is shorter than that of the Si–S bond (~2.2 Å), resulting in bonding between Si and S atoms. This promotes the electronic transfer from SiC–H to MoS_2 (0.097 e) and enhances the bonding between MoS_2 and SiC–H. In addition, the plane-averaged electrostatic potentials of MoS_2 on the SiC nanosheet with or without hydrogenation are calculated and shown in Fig. 3. It can be found that the potential of SiC (8.613 eV) in the MoS_2/SiC heterostructure is deepened (Fig. 3a). The large potential drop of the MoS_2/SiC heterostructure indicates a strong electrostatic field across the interface, which may affect the kinetics of photo-generated carriers. Although the hydrogenated SiC also has a deeper potential than that of MoS_2 in the heterostructure, the potential difference between the hydrogenated SiC and MoS_2 is reduced compared to that between SiC and MoS_2 (Fig. 3b–g).

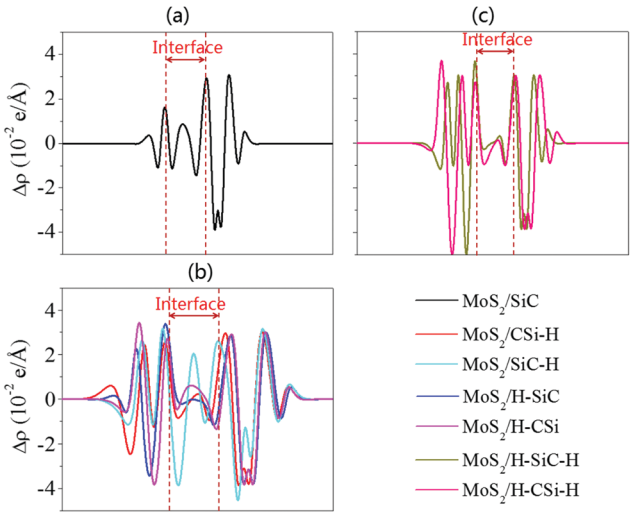

Fig. 2 Averaged charge density difference of MoS_2 on SiC with and without hydrogenation.

3.3. Electronic structures

Generally, the electronic states are sensitive to the interlayer interaction, and the band structure of vertically stacked 2D heterostructures is not a simple superposition of the components. The electronic states of graphene related materials are even remarkably modulated by the weak interlayer interaction.[58,59] For instance, the E_g value is reduced from 1.85 eV to 1.72 eV, and a direct-to-indirect band gap transition occurs, when monolayer MoS_2 is stacked on fully hydrogenated AlN.[29] The isolated MoS_2 and SiC monolayers are semiconductors with direct band gaps of 1.729 eV and 2.558 eV, respectively (Fig. 4a and b).[36,60,61] As for monolayer MoS_2 on SiC, the valence band maximum (VBM) is composed mainly of the states from SiC, while the conduction band minimum (CBM) is composed of the states from MoS_2 (Fig. 4c and d). Although the direct band gap is maintained, the band structure and the E_g value of monolayer MoS_2 change considerably, and MoS_2 is changed into n-type, when attached on SiC. The results indicate substantial interaction between the MoS_2 and SiC sublayers.

The electronic states of monolayer MoS_2 are also quite sensitive to the termination of the hydrogenated SiC. The density of states (DOS) of monolayer MoS_2 on hydrogenated SiC are plotted in Fig. 5. For the monolayer MoS_2 on partially hydrogenated SiC, the ferromagnetic states are preferred for MoS_2/CSi–H, MoS_2/H–SiC and MoS_2/H–CSi heterostructures, but the non-magnetic ground state is preferred in the MoS_2/SiC–H heterostructure (Fig. 5a–d). Spin polarization occurs only

 This journal is © The Royal Society of Chemistry 2018

Published on 05 April 2018. Downloaded by Xian Jiaotong University on 12/26/2019 10:34:25 AM.

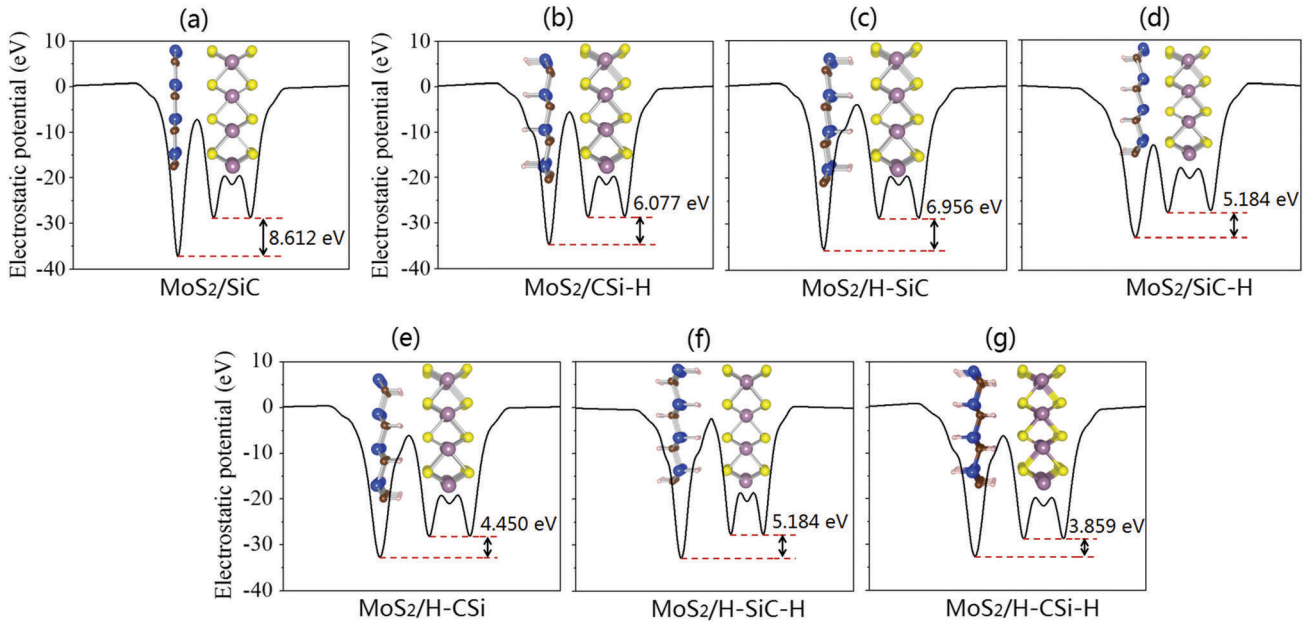

Fig. 3 Averaged electrostatic potential of MoS_2 on SiC with and without hydrogenation.

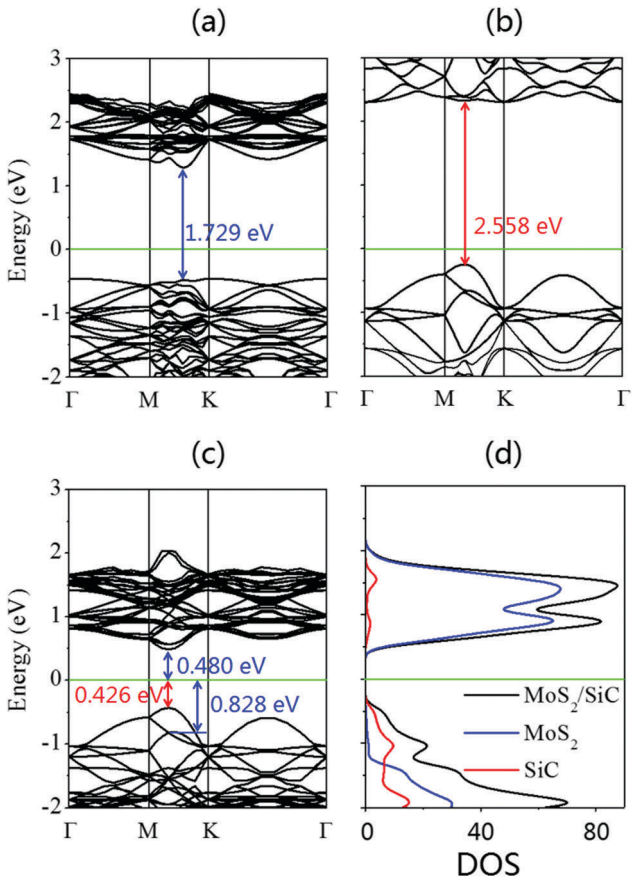

Fig. 4 Energy band structures of (a) monolayer MoS_2 and (b) SiC as well as (c) an MoS_2/SiC heterostructure; (d) total and partial density of states (DOS) of MoS_2/SiC. The Fermi level is set at 0 eV and indicated by the green line.

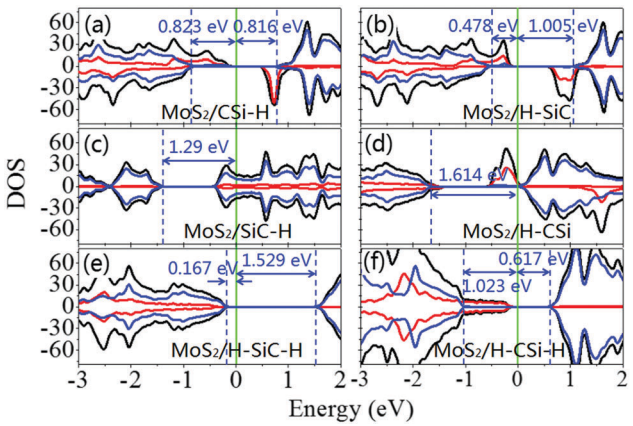

Fig. 5 DOS of monolayer MoS_2 on SiC with hydrogenation. The Fermi level is set at 0 eV and indicated by the green line.

in the partially hydrogenated SiC sheet, but not in the MoS_2 sublayer for which the spin-up and spin-down channels are almost symmetric. This is confirmed by the magnetic density in Fig. S5 (ESI†). Spin polarization emerges on the C and H atoms (Si atoms) in MoS_2/CSi–H and MoS_2/H–SiC (MoS_2/H–CSi) heterostructures, similar to that of partially hydrogenated SiC sheets (Fig. S4c–f, ESI†). Specifically, as for the MoS_2 sublayer in the MoS_2/CSi–H heterostructure, the energy difference between the E_F and the VBM is almost equal to that between the CBM and E_F (Fig. 5a), while for the MoS_2/H–SiC heterostructure, the electronic structure of the MoS_2 sublayer is almost maintained with respect to the isolated monolayer MoS_2 (Fig. 5b). For the MoS_2/H–CSi heterostructure, the E_F shifts towards the CBM of the MoS_2 sublayer, implying that the MoS_2 sublayer is changed into an n-type one (Fig. 5d). The MoS_2/SiC–H heterostructure

Published on 05 April 2018. Downloaded by Xian Jiaotong University on 12/26/2019 10:34:25 AM.

exhibits similar behavior, but the MoS_2 sublayer in the MoS_2/H–SiC heterostructure exhibits a metallic feature (Fig. 5c). As for the MoS_2/H–SiC–H heterostructure, the E_F is slightly above the VBM (0.167 eV) of the MoS_2 sublayer and far away from the CBM (1.529 eV), characteristic of the p-type feature of the MoS_2 sublayer (Fig. 5e). Since MoS_2 is physically absorbed on H–SiC–H, the electronic state of MoS_2 is nearly unperturbed. However, as the dipole of H–SiC–H is rotated by 180° (*i.e.*, MoS_2/H–CSi–H), the E_F is close to the CBM (0.617 eV) of MoS_2, characteristic of the n-type feature of the MoS_2 sublayer (Fig. 5f). The fully hydrogenated SiC can be switched from n- to p-type or *vice versa* for the MoS_2 sublayer by changing the orientation of the intrinsic dipole moment.

To understand the role of the termination surface of SiC, a model of a hydrogenated monolayer SiC sandwiched by two monolayer MoS_2 (MoS_2/H–SiC–H/MoS_2) is built, as shown in Fig. 6a. Although the interlayer distance between the bottom and top MoS_2 on H–SiC–H is different (d_1 = 2.899 Å and d_2 = 2.270 Å), the Mo–S bond lengths in the bottom and top MoS_2 sublayers (L_{Mo-S} = 2.408 Å) are equal to each other. The structural parameters change little, but the binding energy (E_b = −405 meV) is lower than that of MoS_2 on fully hydrogenated SiC by 80%. Fig. 6b shows the DOS projected on the bottom MoS_2, H–SiC–H, and top MoS_2 sublayers. For the MoS_2/H–SiC–H/MoS_2 trilayer heterostructure, the VBM is mainly contributed by the bottom MoS_2 sublayer, whereas the CBM is dominated by the electronic states from the top MoS_2 sublayer. The potential difference across the fully hydrogenated SiC sheet breaks the interfacial symmetry, resulting in a p-type (n-type) doping in the bottom (top) monolayer MoS_2. So bipolar doping might be induced without an external electric field being applied. As shown in Fig. 6c, the charge is substantially redistributed. The plane-averaged charge density difference in the MoS_2/H–SiC–H/MoS_2 heterostructure seems to be a sum of those of MoS_2/H–SiC–H and MoS_2/H–CSi–H. The charge transfer leads to a significant potential difference of 1.426 eV between the bottom and top MoS_2 monolayers (Fig. 6d). So a dipole moment from the top monolayer MoS_2 to the bottom one is generated. Accordingly, p–n junctions, field effect transistors and logic devices might be designed.

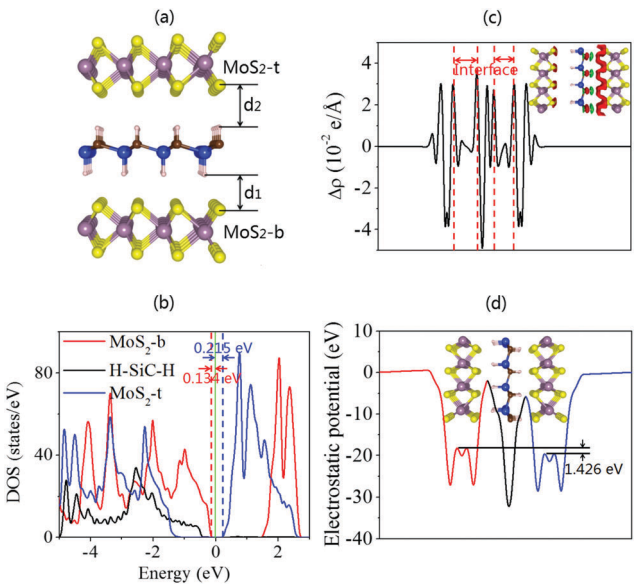

Fig. 6 (a) Optimized structure of bilayer MoS_2 separated by a fully hydrogenated SiC sheet (MoS_2/H–SiC–H/MoS_2). (b) DOS projected on bottom MoS_2, H–SiC–H, and top MoS_2 in an MoS_2/H–SiC–H/MoS_2 trilayer heterostructure. The Fermi level is set at 0 eV and indicated by the green line. The plane-averaged (c) charge density difference and (d) electrostatic potential of MoS_2/H–SiC–H/MoS_2 trilayer heterostructure. The inset is the 3D isosurface of the charge density difference. The red and green areas represent electrons accumulation and depletion, respectively.

3.4. Transport properties

The MoS_2/H–SiC–H/MoS_2 device is constructed between four layers of Au in the channel region (Fig. 7a). The semi-infinite face-centered cubic Au(111) planes are used as electrodes. Electrodes with different lengths of 4.71 Å, 7.06 Å and 14.13 Å were adopted to study the effect of electrode size on the transport properties of the MoS_2/H–SiC–H/MoS_2 heterostructure. As shown in Fig. 7b, their transmission spectra are almost coincident with each other; that is, they are independent of electrode size because of the semi-infinite electrode used. So as an example, the electrode with a length of 7.06 Å is adopted. First, we examine whether the dipole moment between the bottom and top MoS_2 monolayers is maintained. Although the energy difference is increased, the VBM (CBM) is still mainly contributed by the bottom (top) MoS_2 sublayer for the MoS_2/H–SiC–H/MoS_2 trilayer heterostructure in the channel region (Fig. S6, ESI†). The Schottky barrier is evaluated from the DOS of MoS_2 to be 0.527 eV and 0.728 eV for electron and hole, respectively. Fig. 7b shows the transmission spectra of the MoS_2–H–SiC–H–MoS_2 trilayer heterostructure under zero bias, which is consistent with the electronic properties. The drain-source current of the MoS_2–H–SiC–H–MoS_2 trilayer heterostructure under a bias voltage is calculated, and the results are shown in Fig. 7c. The MoS_2–H–SiC–H–MoS_2 system exhibits current rectification, characteristic of a p–n junction.

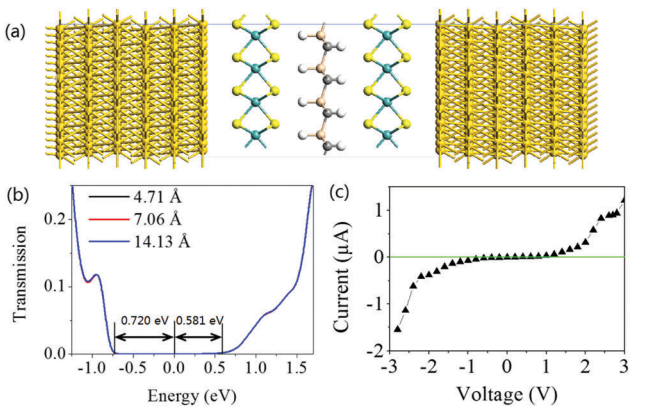

Fig. 7 Transfer characteristics of the MoS_2/H–SiC–H/MoS_2 trilayer heterostructure with Au electrodes: (a) optimized structure of the MoS_2/H–SiC–H/MoS_2 trilayer heterostructure by constructing between six layers of Au, (b) transmission spectrum under zero bias, and (c) *I*–*V* curve.

This journal is © The Royal Society of Chemistry 2018

Published on 05 April 2018. Downloaded by Xian Jiaotong University on 12/26/2019 10:34:25 AM.

4. Conclusions

First-principles calculations are performed to study the influences of a hydrogenated SiC sublayer on the electronic states and charge transfer in monolayer MoS_2 stacked on an SiC sheet. It is found that monolayer MoS_2 exhibits metallic characteristics when in contact with the Si termination of SiC–H (MoS_2/SiC–H), but exhibits ambipolar type polarization when in contact with the C termination of CSi–H (MoS_2/CSi–H). Furthermore, monolayer MoS_2 can be switched from p-type on H-Si terminations (MoS_2/H–SiC and MoS_2/H–SiC–H) to n-type on H–C terminations (MoS_2/H–CSi and MoS_2/H–CSi–H). In an MoS_2/H–SiC–H/MoS_2 trilayer heterostructure, of which the fully hydrogenated SiC is sandwiched between two monolayer MoS_2, charge transfer between the top or bottom MoS_2 sublayer and SiC occurs, resulting in p–n junctions. This implies that the electronic states of monolayer MoS_2 on an SiC sheet can be substantially tuned through hydrogenation and a p–n junction might be produced in the 2D heterostructure, which is crucial for electronic device applications.

Conflicts of interest

There are no conflicts to declare.

Acknowledgements

This work was jointly supported by National Natural Science Foundation of China (Grant No. 51771144, 51471130, 51501012), Natural Science Foundation of Shaanxi Province (No. 2017JZ015), Fund of the State Key Laboratory of Solidification Processing in NWPU (SKLSP201708), Fundamental Research Funds for the Central Universities. This work was carried out at HPCC Platform in Xian Jiaotong University.

References

1 K. S. Novoselov, A. K. Geim, S. V. Morozov, D. Jiang, Y. Zhang, S. V. Dubonos, I. V. Grigorieva and A. A. Firsov, *Science*, 2004, **306**, 666–669.
2 S. Z. Butler, S. M. Hollen, L. Cao, Y. Cui, J. A. Gupta, H. R. Gutiérrez, T. F. Heinz, S. S. Hong, J. Huang, A. F. Ismach, E. Johnston-Halperin, M. Kuno, V. V. Plashnitsa, R. D. Robinson, R. S. Ruoff, S. Salahuddin, J. Shan, L. Shi, M. G. Spencer, M. Terrones, W. Windl and J. E. Goldberger, *ACS Nano*, 2013, **7**, 2898–2926.
3 Q. H. Wang, K. Kalantar-Zadeh, A. Kis, J. N. Coleman and M. S. Stano, *Nat. Nanotechnol.*, 2012, **7**, 699–712.
4 M. Xu, T. Liang, M. Shi and H. Chen, *Chem. Rev.*, 2013, **113**, 3766–3798.
5 H. R. Gutierrez, *Nano Lett.*, 2013, **13**, 3447–3454.
6 K. F. Mak, C. Lee, J. Hone, J. Shan and T. F. Heinz, *Phys. Rev. Lett.*, 2010, **105**, 136805.
7 S. Najmaei, Z. Liu, W. Zhou, X. L. Zou, G. Shi, S. D. Lei, B. I. Yakobson, J. C. Idrobo, P. M. Ajayan and J. Lou, *Nat. Mater.*, 2013, **12**, 754–759.
8 A. M. Van der Zande, P. Y. Huang, D. A. Chenet, T. C. Berkelbach, Y. M. You, G. H. Lee, T. F. Heinz, D. R. Reichman, D. A. Muller and J. C. Hone, *Nat. Mater.*, 2013, **12**, 554–561.
9 J. N. Coleman, M. Lotya, A. O'Neill, S. D. Bergin, P. J. King, U. Khan, K. Young, A. Gaucher, S. De, R. J. Smith, I. V. Shvets, S. K. Arora, G. Stanton, H. Y. Kim, K. Lee, G. T. Kim, G. S. Duesberg, T. Hallam, J. J. Boland, J. J. Wang, J. F. Donegan, J. C. Grunlan, G. Moriaty, A. Shmeliov, R. J. Nicholls, J. M. Perkins, E. M. Grieveson, K. Theuwissen, D. W. McComb, P. D. Nellist and V. Nicolosi., *Science*, 2011, **331**, 568–571.
10 H. Sahin, S. Cahangirov, M. Topsakal, E. Bekaroglu, E. Akturk, R. T. Senger and S. Ciraci, *Phys. Rev. B: Condens. Matter Mater. Phys.*, 2009, **80**, 155453.
11 S. S. Lin, *J. Phys. Chem. C*, 2012, **116**, 3951–3955.
12 X. L. Sui, C. Si, B. Shao, X. L. Zou, J. Wu, B. L. Gu and W. H. Duan, *J. Phys. Chem. C*, 2015, **119**, 10059–10063.
13 A. Hashmi and J. Hong, *J. Phys. Chem. C*, 2015, **119**, 9198–9204.
14 B. Radisavljevic, A. Radenovic, J. Brivio, V. Giacometti and A. Kis, *Nat. Nanotechnol.*, 2011, **6**, 147–150.
15 C. Ahn, J. Lee, H.-U. Kim, H. Bark, M. Jeon, G. H. Ryu, Z. Lee, G. Y. Yeom, K. Kim, J. Jung, Y. Kim, C. Lee and T. Kim, *Adv. Mater.*, 2015, **27**, 5223–5229.
16 S. Kim, A. Konar, W.-S. Hwang, J. H. Lee, J. Lee, J. Yang, C. Jung, H. Kim, J.-B. Yoo, J.-Y. Choi, Y. W. Jin, S. Y. Lee, D. Jena, W. Choi and K. Kim, *Nat. Commun.*, 2012, **3**, 1011.
17 B. Radisavljevic, M. B. Whitwich and A. Kis, *ACS Nano*, 2011, **5**, 9934–9938.
18 H. Wang, L. Yu, Y.-H. Lee, Y. Shi, A. Hsu, M. L. Chin, L.-J. Li, M. Dubey, J. Kong and T. Palacios, *Nano Lett.*, 2012, **12**, 4674–4680.
19 A. Pospischil, M. M. Furchi and T. Mueller, *Nat. Nanotechnol.*, 2014, **9**, 257–261.
20 B. W. H. Baugher, H. O. H. Churchill, Y. Yang and P. Jarillo-Herrero, *Nat. Nanotechnol.*, 2014, **9**, 262–267.
21 J. S. Ross, P. Kiement, A. M. Jones, N. J. Ghimire, J. Q. Yan, D. G. Mandrus, T. Taniguchi, K. Watanabe, K. Kitamura, W. Yao, D. H. Cobden and X. D. Xu, *Nat. Nanotechnol.*, 2014, **9**, 268–272.
22 C. H. Lee, G. H. Lee, A. M. van der Zande, W. C. Chem, Y. L. Li, M. Y. Han, X. Cui, G. Arefe, C. Nuckolls, T. F. Heinz, J. Guo, J. Hone and P. Kim, *Nat. Nanotechnol.*, 2014, **9**, 676–681.
23 R. Cheng, D. H. Li, H. L. Zhou, C. Wang, A. X. Yin, S. Jiang, Y. Liu, Y. Chen, Y. Huang and X. F. Duan, *Nano Lett.*, 2014, **14**, 5590–5597.
24 M. H. Chiu, C. D. Zhang, H. W. Shiu, C. P. Chuu, C. H. Chen, C. Y. S. Chang, C. H. Chen, M. Y. Chou, C. K. Shih and L. J. Li, *Nat. Commun.*, 2015, **6**, 7666.
25 H. Bhunia, A. Bera and A. J. Pal, *ACS Appl. Mater. Interfaces*, 2017, **9**, 8248–8254.
26 N. J. Borys, M. J. Walter, J. Huang, D. V. Talapin and J. M. Lupton, *Science*, 2010, **330**, 1371–1374.
27 W. Seidel, A. Titkov, J. P. André and M. Voos, *Phys. Rev. Lett.*, 1994, **73**, 2356–2359.

Published on 05 April 2018. Downloaded by Xian Jiaotong University on 12/26/2019 10:34:25 AM.

28 D. Çakir and F. M. Peeters, *Phys. Chem. Chem. Phys.*, 2015, **17**, 27636–27641.
29 C. He, W. X. Zhang, T. Li, L. Zhao and X. G. Wang, *Phys. Chem. Chem. Phys.*, 2015, **17**, 23207–23213.
30 E. Bekaroglu, M. Topsakal, S. Cahangirow and S. Ciraci, *Phys. Rev. B: Condens. Matter Mater. Phys.*, 2010, **81**, 075433.
31 E. W. Lee II, L. Ma, D. N. Nath, C. H. Lee, A. Arehart, Y. Y. Wu and S. Rajan, *Appl. Phys. Lett.*, 2014, **105**, 203504.
32 X. N. Guo, X. Tang, Y. W. Wang, C. M. Che, G. Q. Jin and X. Y. Guo, *J. Mater. Chem. A*, 2013, **1**, 4657–4661.
33 Y. Ma, L. Kou, A. Du and T. Heine, *Nano Res.*, 2015, **8**, 3412–3420.
34 S. B. Tang and X. R. Cao, *Phys. Chem. Chem. Phys.*, 2014, **16**, 23214–23223.
35 S. Tang, J. Yu and L. Liu, *Phys. Chem. Chem. Phys.*, 2013, **15**, 5067–5077.
36 X. P. Chen, J. K. Jiang, Q. H. Liang, R. S. Meng, C. J. Tan, Q. Yang, S. L. Zhang and H. B. Zeng, *J. Mater. Chem. C*, 2016, **4**, 7406–7414.
37 G. Kresse and J. Hafner, *Phys. Rev. B: Condens. Matter Mater. Phys.*, 1993, **47**, 558–561.
38 G. Kresse and J. Hafner, *Phys. Rev. B: Condens. Matter Mater. Phys.*, 1994, **49**, 14251–14269.
39 P. E. Blöchl, *Phys. Rev. B: Condens. Matter Mater. Phys.*, 1994, **50**, 17953–17979.
40 J. P. Perdew, K. Burke and M. Ernzerhof, *Phys. Rev. Lett.*, 1996, **77**, 3865–3868.
41 *Gmelin Handbook of Inorganic and Organometallic Chemistry*, Springer-Verlag, Berlin, 8th edn, 1995, vol. B7.
42 M. A. L. Marques, J. Vidal, M. J. T. Oliveira, L. Reining and S. Botti, *Phys. Rev. B: Condens. Matter Mater. Phys.*, 2011, **83**, 035199.
43 S. Lebègue and O. Eriksson, *Phys. Rev. B: Condens. Matter Mater. Phys.*, 2009, **79**, 115409.
44 C. Ataca and S. Ciraci, *J. Phys. Chem. C*, 2011, **115**, 13303.
45 A. Ramasubramaniam, D. Naveh and E. Towe, *Phys. Rev. B: Condens. Matter Mater. Phys.*, 2011, **84**, 205325.
46 F. Tran and P. Blaha, *Phys. Rev. Lett.*, 2009, **102**, 226401.
47 S. Bhattacharyya and A. K. Singh, *Phys. Rev. B: Condens. Matter Mater. Phys.*, 2012, **86**, 075454.
48 S. Grimme, *J. Comput. Chem.*, 2006, **27**, 1787–1799.
49 K. Momma and F. Izumi, *J. Appl. Crystallogr.*, 2008, **41**, 653–658.
50 M. Brandbyge, J.-L. Mozos, P. Ordejón, J. Taylor and K. Stokbro, *Phys. Rev. B: Condens. Matter Mater. Phys.*, 2002, **65**, 165401.
51 M. S. José, A. Emilio, D. G. Julian, G. Alberto, J. Javier, O. Pablo and S.-P. Daniel, *J. Phys.: Condens. Matter*, 2002, **14**, 2745–2779.
52 D. Çakır and F. M. Peeters, *Phys. Rev. B: Condens. Matter Mater. Phys.*, 2014, **89**, 245403.
53 W. S. Yun, S. W. Han, S. C. Hong, I. G. Kim and J. D. Lee, *Phys. Rev. B: Condens. Matter Mater. Phys.*, 2012, **85**, 033305.
54 X. D. Li, S. Q. Wu and Z. Z. Zhu, *J. Mater. Chem. C*, 2015, **3**, 9403–9411.
55 X. Q. Wang and J. T. Wang, *Phys. Lett. A*, 2011, **375**, 2676–2679.
56 D. S. Koda, F. Bechstedt, M. Marques and L. K. Teles, *J. Phys. Chem. C*, 2017, **121**, 3862–3869.
57 M. S. Zhu, S. Kim, L. Mao, M. Fujitsuka, J. Y. Zhang, X. C. Wang and T. Majima, *J. Am. Chem. Soc.*, 2017, **139**, 13234–13242.
58 S. Li, Y. F. Wu, W. Liu and Y. H. Zhao, *Chem. Phys. Lett.*, 2014, **609**, 161–166.
59 N. Gao, J. C. Li and Q. Jiang, *Phys. Chem. Chem. Phys.*, 2014, **16**, 11673–11678.
60 H. Zhang, Y. N. Zhang, H. Liu and L. M. Liu, *J. Mater. Chem. A*, 2014, **2**, 15389–15395.
61 J. M. Liao, B. S. Sa, J. Zhou, R. Ahuja and Z. M. Sun, *J. Phys. Chem. C*, 2014, **118**, 17594–17599.

 This journal is © The Royal Society of Chemistry 2018